Nuclear Engineering and Technology 58 (2026) 104178

Contents lists available at ScienceDirect

Nuclear Engineering and Technology

journal homepage: www.elsevier.com/locate/net

Original Article

Improved reduced order modelling for time-dependent fission gas diffusion in columnar grains tailored for fuel performance applications

M. Di Gennaro [a], D. Pizzocri [a,*], F.A.B. Silva [b], G. Zullo [a], S. Lorenzi [a], A. Cammi [c,a], L. Luzzi [a]

[a] Politecnico di Milano, Department of Energy, Nuclear Engineering Division, Via La Masa 34, 20156, Milano, Italy
[b] Texas A&M University, Department of Nuclear Engineering, TX 77843-3133, College Station, United States of America
[c] Emirates Nuclear Technology Center (ENTC), Department of Mechanical and Nuclear Engineering, Khalifa University, Abu Dhabi, 127788, United Arab Emirates

ARTICLE INFO

Keywords:
Fission gas diffusion
Physics-based modelling
Columnar grains
Reduced order modelling
Proper orthogonal decomposition

ABSTRACT

At the beginning of irradiation, fast reactors experience a radical alteration of fuel micro-structure driven by high temperatures and steep temperature gradients, leading to the formation of columnar grains. It is common in fuel performance codes to model fission gas diffusion in the columnar grain zone by approximating fuel grains as spherical, using a representative radius for the cylindrical geometry and assuming a uniform temperature, thereby neglecting the temperature gradient. However, the distinct diffusion kinetics induced by the temperature gradient render this classical approach unsuitable, resulting in inaccurate estimations of gas release. To account for the non-spheroidal shape and the effects of the temperature gradient in fission gas modules of conventional fuel performance codes, a previous work by the same authors proposed a physics-based model to solve the gas diffusion problem in cylindrical grains using reduced order modelling techniques. Building on this prior framework, the present work introduces an advanced reduced order modelling approach that addresses specific limitations of the earlier model. Results highlight the accuracy of the proposed model in both transient and steady-state conditions, while maintaining a computational cost comparable to that of grain-scale fission gas behaviour modules, making it suitable for integration into fuel performance simulations.

1. Introduction

During the initial stages of reactor operation, oxide fuels (UO_2 and MOX) undergo significant alterations in their microstructure, leading to recrystallization of the fuel matrix and changes in grain morphology [1–3]. This restructuring phenomenon primarily affects MOX fuel irradiated under fast reactor conditions, particularly at high linear heating rates (>35 kW m^{-1}), due to the elevated temperatures and steep temperature gradients (with the hottest region at the center of the pellet and the coolest near the cladding) reaching up to 200 K mm^{-1} [4,5].

Restructuring is accompanied by the migration of fabricated porosity along the temperature gradient through an evaporation-condensation mechanism, resulting in the formation of a central void surrounded by a high-density annular zone. During this migration, larger pores become unstable and take on a cigar-like shape as they move, contributing to the formation of radially oriented columnar grains (with grain lengths ranging from approximately 100 μm to 1 mm) towards the central void. Adjacent to the columnar grain region, a zone of large equiaxed grains forms, reflecting significant growth compared to un-irradiated samples (with grain sizes around 20 μm). Finally, the outer rim of the fuel pellet, where the temperature is too low for substantial restructuring, retains the original microstructure of the sintered pellet [6,7].

Modifications in grain morphology have significant effects on material properties and the performance of fuel pellets [8,9]. This study specifically addresses the modelling of intra-granular fission gas diffusion, a critical step in accurately predicting gaseous fuel swelling and fission gas release within the fuel-cladding gap.

Physics-based models for intra-granular fission gas diffusion, either directly embedded in engineering-scale fuel performance codes or supplied by dedicated grain-scale fission gas behaviour modules coupled to them, typically rely on the classical approximation proposed by Booth in [10]. This widely used approach assumes a spherical grain shape with a sufficiently small size to maintain uniform temperature and a consistent fission rate throughout the grain. This approximation is typically applied when studying diffusion in the columnar grain region by tuning the equivalent spherical grain radius to match the asymptotic average concentration in the columnar geometry. However,

* Corresponding author.
E-mail address: davide.pizzocri@polimi.it (D. Pizzocri).

https://doi.org/10.1016/j.net.2026.104178
Received 21 May 2025; Received in revised form 7 January 2026; Accepted 1 February 2026
Available online 6 February 2026

as discussed in a recent work by the same authors [11], this treatment introduces two significant limitations: it fails to capture the distinct diffusion dynamics in cylindrical geometries and neglects the steep temperature gradient characteristic of columnar grains. A fully coupled solution of the fission gas diffusion and energy partial differential equations (PDEs) for individual grains could overcome these limitations, but such an approach would require computational resources incompatible with the efficiency demands of current engineering-scale fuel performance codes.

In our previous work [11], we proposed an alternative approach for modelling the temporal evolution of fission gas diffusion in columnar grains by adopting reduced order modelling techniques. This study demonstrated the feasibility of accounting for both the non-spheroidal shape and the temperature distribution along the grain while maintaining a computational cost comparable to that of grain-scale fission gas behaviour modules. As a result, this approach is well-suited for integration into fuel performance simulations.

In this work, we propose an advanced reduced order modelling technique that addresses specific limitations of the previous approach, improving accuracy and ensuring more robust predictions. While retaining the intrusive nature of the method, the use of the Galerkin projection, and the division into an Offline/Online procedure, the new approach includes two essential new ingredients: (i) the adoption of the discretized empirical interpolation method (DEIM) [12] to efficiently handle the nonlinearity associated with the diffusion coefficient; (ii) the construction of the surrogate model using a broader parameter set, ensuring applicability across a wide range of operating conditions encountered in fuel performance code simulations. Mode selection continues to be performed using proper orthogonal decomposition (POD) [13–15], but, due to the broader parameter space, we now employ a POD-greedy algorithm to ensure optimal mode selection across the entire parameter range.

Consistently with the assumptions made in the previous study, this work focuses exclusively on fully-formed columnar grains, assuming that the restructuring and grain formation processes have already occurred. As a result, early-stage phenomena such as grain boundary sweeping [16] — during which fission gases accumulate at moving grain boundaries, effectively preventing intra-granular gas diffusion — are not considered in the present model.

The Offline phase is performed in Python, using a finite element discretization of the computational domain implemented in FreeFEM++ [17]. The Online phase, on the other hand, is implemented in the 0D grain-scale code SCIANTIX for physics-based modelling of fission gases in nuclear oxide fuels [18,19], which is already coupled with fuel performance codes [20,21].

The remainder of this paper is organized as follows. In Section 2, we present the mathematical formulation and the full-order approximation of the intra-granular fission gas diffusion problem. In Section 3, the reduced order methodology is introduced and discussed in detail. Section 4 focuses on testing the reduced order modelling technique against the full order solution, while Section 5 provides a deeper analysis of the errors and computational costs, offering further insights into the efficiency and accuracy of the proposed approach. Finally, Section 6 resents the conclusions and perspectives, outlining directions for future improvements and developments.

2. Mathematical formulation and full order approximation

In the following sections, we provide a comprehensive description of the physical phenomenon under study and the domain discretization scheme used.

2.1. Governing equations

To simulate the diffusion of fission gases in columnar grains, we use two partial differential equations that model the temperature and concentration fields. Let $\Omega \subset \mathbb{R}^3$ denote the spatial domain (Fig. 1), whose boundary is denoted by $\partial\Omega = \Gamma_1 \cup \Gamma_2 \cup \Gamma_3$, where each Γ_i corresponds to a portion of the domain boundary described below, and let $\mathcal{I} := (t_0, t_{N_t}]$ represent the observation time interval, where $t_0, t_{N_t} > t_0 \in \mathbb{R}$ are the initial and final time values, respectively, with N_t being the number of time steps. The problem consists of finding the scalar concentration field c (atm m^{-3}) such that

$$\begin{cases} \rho c_p \partial_t T - \nabla \cdot (\boldsymbol{k} \nabla T) = \dot{F} E_{fiss} & \text{on } \Omega \times \mathcal{I}, \quad (1a) \\ -\boldsymbol{k} \nabla T \cdot \boldsymbol{n} = 0 & \text{on } \Gamma_2 \times \mathcal{I}, \Gamma_3 \times \mathcal{I}, \quad (1b) \\ T = T_{BC} & \text{on } \Gamma_1 \times \mathcal{I}, \quad (1c) \\ T(t_0) = T_{IC} & \text{on } \Omega, \quad (1d) \\ \partial_t c - \nabla \cdot (\boldsymbol{D}(T) \nabla c) = \dot{F} \gamma & \text{on } \Omega \times \mathcal{I}, \quad (1e) \\ c = 0 & \text{on } \partial\Omega \times \mathcal{I}, \quad (1f) \\ c(t_0) = 0 & \text{on } \Omega. \quad (1g) \end{cases}$$

where ρ is the density (kg m^{-3}), c_p is the specific heat (J kg^{-1} K^{-1}), k is the thermal conductivity (W m^{-1} K^{-1}),[1] $\dot{F}$ is the fission rate (fiss m^{-3} s^{-1}),[2] E_{fiss} is the energy released per nuclear fission (J fiss^{-1}), $\boldsymbol{D}$ is the intra-granular diffusion coefficient (m^2 s^{-1}), γ is the fission yield (at fiss^{-1}). In the fifth equation in System (1), the quasi-stationary approach proposed by [30] is adopted, in which the trapping and resolution rates of gas atoms to and from intra-granular bubbles are lumped into an effective diffusion coefficient (fully described in [19]). As a result, the problem is reformulated as a purely diffusive one, where the diffusion coefficient $\boldsymbol{D}$ already accounts for these underlying microstructural interactions.

The temperature PDE (Eq. (1a)) is completed with a Dirichlet boundary condition T_{BC} (K) on Γ_1 (Eq. (1c)), which represents the surface at the interface with the equiaxed grains region. Zero Neumann boundary conditions are applied on Γ_2 and Γ_3 (Eq. (1b)), corresponding to the lateral surface and the surface at the interface with the central void of the pellet, respectively. For the concentration PDE (Eq. (1e)), the grain boundary surface acts as a *perfect sink*, leading to a boundary condition of zero gas concentration directly adjacent to the grain boundary (Eq. (1f)). The initial conditions are as follows: the temperature T_{IC} is uniformly set to T_{BC} (Eq. (1d)), the value at the interface with the equiaxed grains region, and the initial concentration is uniformly set to zero throughout the domain (Eq. (1g)).

[1] In this work, the thermal conductivity is assumed to be uniform across the columnar grain region. While it is known that the thermal conductivity of oxide fuels depends on temperature, this assumption is introduced to simplify the current analysis. According to the model proposed in [22] for americium-bearing oxide fuels, over a typical temperature gradient of approximately 200 K mm^{-1}, the local variation in thermal conductivity can reach up to 25%, particularly in the low-temperature range (500–1000 K). This simplification is recognized as a limitation of the model and could be addressed in future work by incorporating temperature-dependent thermal conductivity.

[2] Although the fission rate in fast reactors typically varies along the radial direction of the pellet, particularly near the center due to plutonium redistribution, this analysis assumes it to be constant. This assumption is justified by the fact that the radial variation in volumetric power density is generally small, typically only a few percent. For instance, in the SUPERFACT-1 experiment, the variation in the fission rate is approximately 15% [23,24], which has a minimal impact on the overall solution. Furthermore, in the regions where columnar grains form, typically characterized by higher temperatures, the effect of the fission rate on the diffusion coefficient becomes negligible [25]. Additionally, some fuel performance codes, such as TRANSURANUS [26,27] and FRAPCON [28], employ diffusivity models that do not explicitly depend on the fission rate [29].

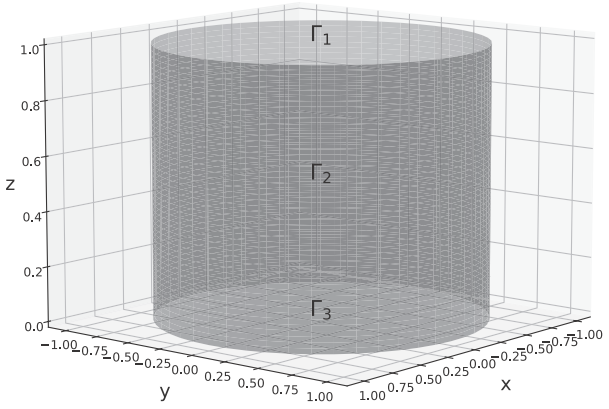

Fig. 1. Sketch of the computational domain used in this work to approximate the columnar grain, with the boundary subdivisions. The z-axis represents the axial direction along the columnar grain axis, corresponding to the radial position within the fuel pellet. Γ_1 denotes the surface adjacent to the equiaxed grain region, Γ_2 is the lateral surface and Γ_3 is the surface adjacent to the central void of the pellet.

In this work, the physical geometry of the grains, defined by their length L and radius R, is mapped onto a unitary reference domain (Fig. 1) to facilitate model order reduction. Columnar grains, typically characterized by a length much greater than their radius, exhibit inherent anisotropy in both heat and mass transport. To preserve the underlying physics of the problem on this reference domain, the transport coefficients are rescaled differently along the radial and axial directions. This results in effective anisotropic conduction and diffusion tensors, expressed through the transformed heat transfer coefficient $\boldsymbol{k} = \text{diag}\left(\frac{k}{R^2}, \frac{k}{R^2}, \frac{k}{L^2}\right)$ and mass transfer coefficient $\boldsymbol{D}(T) = \text{diag}\left(\frac{D(T)}{R^2}, \frac{D(T)}{R^2}, \frac{D(T)}{L^2}\right)$.

Based on the analysis presented in [11], a comparison of the timescales of the phenomena involved revealed that the temperature dynamics are significantly faster, by six orders of magnitude, than the evolution of the concentration field. Specifically, the temperature stabilizes on the order of seconds, whereas the concentration field evolves over timescales of 10^6 s. As a result, it is reasonable to assume a steady-state solution for the temperature. This asymptotic behaviour can be approximated, for large t, by the leading term of the series expansion of the solution:

$$T_\infty = \frac{\dot{F} E_{fiss} L^2}{2k}(1 - z^2) + T_{IC} \tag{2}$$

The temperature field is uniform along the radial direction and is primarily a function of the axial coordinate z only, leading to the one-dimensional steady-state profile given by Eq. (2).

It is important to underline that the intra-granular diffusion model in Eq. (1) alone is not exhaustive and must be coupled with a consistent model for the inter-granular behaviour to provide a complete description of fission gas behaviour.

2.2. Finite element approximation

The weak formulation of the problem consists of finding $c \in H_0^1(\Omega)$ such that for all $v \in H_0^1(\Omega)$

$$\int_\Omega \frac{\partial c}{\partial t} \cdot v d\Omega + \int_\Omega \boldsymbol{D}(T)\nabla c \cdot \nabla v d\Omega = \dot{F}\gamma \int_\Omega v d\Omega \tag{3}$$

Given the axial symmetry of the problem, we solve it in cylindrical coordinates by considering only the spatial domain $\tilde{\Omega} = [0,1]^2$. The domain $\tilde{\Omega}$ is discretized into a triangulation $\mathcal{T}_h$, where $\tilde{\Omega} = \cup_{i=1}^{N_h} K_i$, $K_i \in \mathcal{T}_h$. The system of equations, along with their boundary and initial conditions, can then be approximated at the full order level using the finite element method.

$$\int_0^{2\pi} d\phi \iint_0^1 \frac{\partial c_h}{\partial t} v_h r dr dz + \int_0^{2\pi} d\phi \iint_0^1 \frac{D(T)}{R^2} \frac{\partial c_h}{\partial r} \frac{\partial v_h}{\partial r} + \frac{D(T)}{L^2} \frac{\partial c_h}{\partial z} \frac{\partial v_h}{\partial z} r dr dz = \dot{F}\gamma \int_0^{2\pi} d\phi \iint_0^1 v_h r dr dz \tag{4}$$

with ϕ the azimuthal coordinate, r the radial coordinate and $c_h \in \mathcal{V}_h \subset H_0^1(\Omega)$ with $\mathcal{V}_h$ a function (Hilbert) space[3] on $\tilde{\Omega}$ of finite dimension $N_h \in \mathbb{N}^+$

$$\mathcal{V}_h := \{v_h \in H_0^1(\tilde{\Omega}) | \forall K \in \mathcal{T}_h, v|_K \in \mathbb{P}_1\} \tag{5}$$

In this work, the open-source finite element software, FreeFEM++ [17] is used to discretize the computational domain $\tilde{\Omega}$, while the full order simulation is performed in the Python environment (Fig. 2) using an Euler-Backward time discretization scheme. The FEM full order solver used in this work has undergone code verification through mesh and time-step sensitivity analyses, and by cross-comparison with an independent full order OpenFOAM solver developed in our previous study [11]. The agreement was confirmed both in terms of concentration fields and temperature profiles, ensuring high accuracy in the finite element predictions without negatively impacting Online efficiency. The adopted mesh features non-uniform grid refinement (as shown in the [31]), with a finer resolution near the boundaries to capture high-gradient phenomena and a coarser resolution at the center to optimize computational resources. Based on the convergence study, an optimal mesh refinement of $N_h = 10201$ degrees of freedom (101×101 layers) was selected.

3. Reduced order model

As is common in reduced order techniques, the procedure is divided into two phases: an Offline phase, which is computationally more demanding, and an Online phase, which is significantly faster. During the Offline phase, a low-dimensional approximation of the solution space is constructed, and the surrogate model is derived by projecting the full order model (FOM) onto the reduced space. In contrast, the Online phase focuses on efficiently solving the resulting linear system.

In this context, let $\mathcal{P} \subset \mathbb{R}^P$ denote the P-dimensional parameter space, and let $\boldsymbol{\mu} \in \mathcal{P}$ represent the parameters, which in this work are given by $\boldsymbol{\mu} = \{\dot{F}, k, \gamma, R, L, T_{BC}\}$. We define the training set $\Xi_{train} := \{\boldsymbol{\mu}_p\}_{p=1}^{\mathcal{P}} \subset \mathcal{P}$ as a sufficiently rich subset of the parameter space, which can be generated by drawing random samples from a uniform distribution within $\mathcal{P}$, or with other sampling techniques such as latin hypercube sampling or Monte Carlo methods (see [32] for further details).

The spatial basis functions that populate the reduced space $\mathcal{V}_\varepsilon = \text{span}\{\psi_i(\boldsymbol{x})\}_{i=1}^{N_\varepsilon} \subset H_0^1$ are extracted using a POD-greedy approach [33–35], as detailed further in Section 3.2. This method is particularly well-suited for parameterized time-dependent problems, as it combines a greedy selection procedure in the parameter space with the POD applied in time at fixed parameter values. This hybrid approach efficiently handles the temporal component of the solution.

Once the N_ε-dimensional set of spatial reduced basis functions is available, the full order solution $c_h(\boldsymbol{x}, t; \boldsymbol{\mu})$ can be approximated in the reduced space $\mathcal{V}_\varepsilon$ as

$$c_h(\mathbf{x}, t; \boldsymbol{\mu}) \approx c_\varepsilon(\mathbf{x}, t; \boldsymbol{\mu}) = \sum_{i=1}^{N_\varepsilon} \psi_i(\mathbf{x}) \alpha_i(t; \boldsymbol{\mu}), \quad \boldsymbol{x} \in \tilde{\Omega}, t \in \mathcal{I}, \boldsymbol{\mu} \in \mathcal{P} \tag{6}$$

where $\boldsymbol{\alpha}(t, \boldsymbol{\mu}) = (\alpha_1(t, \boldsymbol{\mu}), \dots, \alpha_{N_\varepsilon}(t, \boldsymbol{\mu})) \in \mathbb{R}^{N_\varepsilon \times P}$ denotes the matrix of expansion coefficients in the reduced basis. The concentration equation (Eq. (1e)) can be rewritten as

$$\sum_{i=1}^{N_\varepsilon} \frac{\partial \alpha_i(t; \boldsymbol{\mu})}{\partial t} \boldsymbol{M}_{ij} + \sum_{i=1}^{N_\varepsilon} \alpha_i(t; \boldsymbol{\mu}) \boldsymbol{K}_{ij} = S s_j, \quad j = 1, \dots, N_\varepsilon \tag{7}$$

[3] Equipped with inner product $(\cdot, \cdot)_{H_0^1}$ and induced norm $\|\cdot\|_{H_0^1}$.

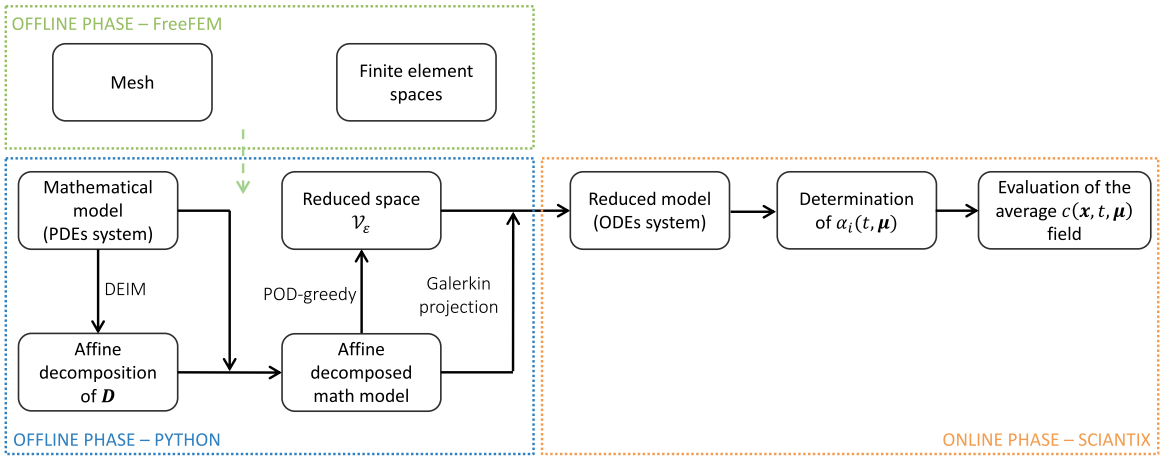

Fig. 2. Illustration of the methodology followed in this work, along with the corresponding code implementation.

Here, S is the concentration source term, defined as the product of the fission rate and the fission yield. The matrices $\boldsymbol{M}, \boldsymbol{K} \in \mathbb{R}^{N_\varepsilon \times N_\varepsilon}$ represent the mass and stiffness matrix, respectively, while the vector $\boldsymbol{s} \in \mathbb{R}^{N_\varepsilon}$ denotes the source vector. These quantities are defined as follows

$$\boldsymbol{M}_{ij} = \int_{\tilde{\Omega}} \psi_i \cdot \psi_j d\tilde{\Omega}, \quad \boldsymbol{K}_{ij}(T) = \int_{\tilde{\Omega}} \boldsymbol{D}(T)(\nabla\psi_i \cdot \nabla\psi_j) d\tilde{\Omega}, \quad \boldsymbol{s}_i = \int_{\tilde{\Omega}} \psi_j d\tilde{\Omega} \tag{8}$$

The diffusion coefficient of fission gases in uranium dioxide or mixed oxide fuels is typically described by an Arrhenius expression [29, 36]. This exponential dependence on temperature leads to a nonaffine (nonlinear) parameter dependency. To recover an approximate affine decomposition and enable an efficient Offline-Online procedure, we adopt the discrete empirical interpolation method (DEIM) [12], as fully described in Section 3.1. The decision to use the discrete variant of the original empirical interpolation method (EIM) [37] is driven by the advantage of generating the basis functions through the POD approach, which is computationally more efficient compared to the EIM-based method, and by its ability to provide better control over the approximation error.

In Fig. 2 the key steps of the approach are outlined. The Offline phase is carried out in the Python environment, while the solution of the reduced model, obtained through projection onto the reduced space, is performed in the SCIANTIX code, as described in Section 3.3.

3.1. DEIM: construction of the affine decomposition

The DEIM method relies on approximating the diffusion coefficient using an interpolation function expressed as

$$\boldsymbol{D}(T) \approx \tilde{\boldsymbol{D}}(\boldsymbol{\mu}, \boldsymbol{x}) = \sum_{k=1}^{N_D} g_k(\boldsymbol{\mu})\zeta_k(\boldsymbol{x}) \quad \boldsymbol{x} \in \tilde{\Omega}, \boldsymbol{\mu} \in \mathcal{P} \tag{9}$$

where the function is constructed as a linear combination of N_D hierarchically chosen basis functions $\{\zeta_k\}_{k=1}^{N_D} \in \mathcal{U}_D \subseteq H_0^1$, and parameter dependent coefficients, $g_k(\boldsymbol{\mu})$. Here, $\mathcal{U}_D$ represents an approximation of the function space that contains $\boldsymbol{D}$. The DEIM approximation treats the continuous domain $\tilde{\Omega}$ as a finite set of discrete points $\{\boldsymbol{x}_l\}_{l=1}^{N_D} \in \tilde{\Omega}$ where the function is interpolated $\boldsymbol{D}(\boldsymbol{\mu}, \boldsymbol{x}_\ell)$ [12].

The selection of the basis functions is performed using the singular value decomposition (SVD) on a set of discrete snapshots of the parametrized function, $\{\boldsymbol{D}_i\}_{i=1}^{P}$. The interpolation points are selected using a greedy algorithm, which incrementally incorporates new points chosen as those where the residual between the input basis ζ_l and its approximation is maximized (Algorithm 1) [32,38].

The affine decomposed mathematical model (Fig. 2) is obtained by rewriting the stiffness matrix (Eq. (8)) as

$$\tilde{\boldsymbol{K}}_{ijk} = \int_{\Omega} \zeta_k \nabla\psi_i \cdot \nabla\psi_j d\Omega \tag{10}$$

where the matrix has dimensions $\tilde{\boldsymbol{K}} \in \mathbb{R}^{N_D \times N_\varepsilon \times N_\varepsilon}$.

Once the basis functions $\zeta_k(\boldsymbol{x})$ are defined, the coefficients $g_k(\boldsymbol{\mu})$ are determined by enforcing the interpolation condition

$$\sum_{k=1}^{N_D} g_k(\boldsymbol{\mu})\zeta_k(\boldsymbol{x}_l) = \boldsymbol{D}(\boldsymbol{\mu}, \boldsymbol{x}_\ell) \quad \ell = 1, \dots, N_D \tag{11}$$

During the Online stage Section 3.3, when new values of the parameter $\boldsymbol{\mu}$ need to be tested, $\boldsymbol{D}(\boldsymbol{\mu}, \boldsymbol{x}_\ell)$ is computed only at the locations identified by the indices $\boldsymbol{x}_\ell$. This procedure enables the exploitation of the affine parameter dependency, which ensures the computational efficiency of the reduced order model (ROM). The problem is efficiently solvable because the basis functions and interpolation points are precomputed, the entries $\boldsymbol{D}(\boldsymbol{\mu}, \boldsymbol{x}_\ell)$ can be rapidly evaluated online, and the matrix of entries $\zeta_k(\boldsymbol{x}_\ell)$ is non-singular [39].

Algorithm 1: DEIM algorithm (Offline stage)

Input: Training set $\Xi_{train} = \{\boldsymbol{\mu}_1, ..., \boldsymbol{\mu}_{N_P}\}$, number of basis functions N_D
Output: $\mathcal{U}_D = \text{span}\{\zeta_1, ..., \zeta_{N_D}\}$ and interpolation points $\{\boldsymbol{x}_1, ..., \boldsymbol{x}_{N_D}\}$
Construct snapshot matrix: $\boldsymbol{Q} = [D(\boldsymbol{\mu}_1), ..., D(\boldsymbol{\mu}_P)]$
Perform the singular value decomposition: $\boldsymbol{Q} = \boldsymbol{Z}\boldsymbol{S}\boldsymbol{V}^T$
Construct rank-N_D approximation basis: $\boldsymbol{Z}_{N_D} = [\zeta_1, ..., \zeta_{N_D}]$
Initialisation:
  Select the first interpolation point: $\boldsymbol{x}_1 = \arg\max_{\boldsymbol{x}\in\Omega} |\zeta_1(\boldsymbol{x})|$
for (ℓ = 2,..., N_D) **do**
  Find m_k such that $\sum_{k=1}^{\ell-1} m_k\zeta_k(\boldsymbol{x}_r) = \zeta_\ell(\boldsymbol{x}_r)$, $r = 1, ..., \ell-1$
  Compute the residual: $\xi_\ell := \zeta_\ell - \sum_{k=1}^{\ell-1} m_k\zeta_k$
  Select the ℓth interpolation point: $\boldsymbol{x}_\ell = \arg\max_{\boldsymbol{x}\in\Omega} |\xi_\ell(\boldsymbol{x})|$

3.2. POD-greedy: construction of the reduced space

The greedy methods (Algorithm 3)[4] incrementally expand the reduced space $\mathcal{V}_\varepsilon$ by incorporating new basis functions corresponding to

[4] Where Id denotes the identity operator and $\Pi_{\mathcal{V}_\varepsilon}$ denotes the orthogonal projection operator onto $\mathcal{V}_\varepsilon$: $\Pi_{\mathcal{V}_\varepsilon} : \mathcal{V}_h \to \mathcal{V}_\varepsilon$ such that $\Pi_{\mathcal{V}_\varepsilon} v = \arg\min_{u\in\mathcal{V}_\varepsilon} \|v - u\|_{L^2} \forall v \in \mathcal{V}_h$.

states not adequately represented by the current model approximation. Starting from the field solution at a given initial parameters value, $\boldsymbol{\mu}^\star$, the optimal POD modes are sampled at some prescribed time intervals (Algorithm 2). This process is repeated until no further basis functions are needed in $\mathcal{V}_\varepsilon$ to ensure that the maximum error introduced by the reduced basis approximation (relative to the full order finite element approximation) is below a desired error tolerance, ϵ_{POD}. The error estimator, denoted by $\Delta_{\mathcal{V}_\varepsilon}$ in Algorithm 3, follows the formulation proposed by [33], specifically tailored for time-dependent parabolic problems with affine parameter dependence.

Algorithm 2: POD (Offline stage)

Input: Orthogonal complements $o(t_k;\boldsymbol{\mu}^\star)$, number of basis functions M_ε
Output: $\mathcal{W}_\varepsilon = \text{span}\{\psi_i\}_{i=1}^{M_\varepsilon}$
Compute the Gramian matrix of entries
$\boldsymbol{G}_{ij} = \int_\Omega o(t_i;\boldsymbol{\mu}^\star) o(t_j;\boldsymbol{\mu}^\star) d\Omega$
Compute the singular value decomposition: $\boldsymbol{G} = \boldsymbol{A}\boldsymbol{R}\boldsymbol{A}^T$
Construct the basis: $\psi_i = \sum_{k=1}^{N_t} R_{ii}^{-1/2} A_{k,i} o(t_k,\mu^\star)\ \forall i = 1,...,M_\varepsilon$
$\mathcal{W}_\varepsilon = \text{span}\{\psi_k\}_{k=1}^{M_\varepsilon}$

Algorithm 3: POD-greedy (Offline stage)

Input: Training set $\Xi_{train} = \{\boldsymbol{\mu}_1,...,\boldsymbol{\mu}_{N_P}\}$, starting parameters $\boldsymbol{\mu}^\star \in \mathcal{P}$, absolute tolerance ϵ_{POD}, time discretization $\{t_1,...,t_{N_t}\}$
Output: $\mathcal{V}_\varepsilon = \text{span}\{\psi_i\}_{i=1}^{N_\varepsilon}$
Space initialisation: $\mathcal{V}_\varepsilon = \varnothing$, $M_\varepsilon = 1$, $N_\varepsilon = 0$
while $\Delta_{\mathcal{V}_\varepsilon}(\boldsymbol{\mu}^\star) > \epsilon_{POD}$ **do**
  Snapshots extraction: $\{c_h(t_k;\boldsymbol{\mu}^\star)\}_{k=1}^{N_t}$
  Compute the orthogonal complements:
  $o(t_k;\boldsymbol{\mu}^\star) = \text{Id} - \Pi_{\mathcal{V}_\varepsilon}(c_h(t_k;\boldsymbol{\mu}^\star))\ \forall k = 1,...,N_t$
  Select the new basis function: $\mathcal{W}_\varepsilon = \text{POD}(\{o(t_k;\boldsymbol{\mu}^\star)\}_{k=1}^{N_t}, 1)$
  Reduced basis expansion: $\mathcal{V}_\varepsilon = \text{span}(\mathcal{V}_\varepsilon, \mathcal{W}_\varepsilon)$
  Identification of parameters leading to the worst approximated trajectory: $\boldsymbol{\mu}^\star = \arg\max_{\boldsymbol{\mu}\in\mathcal{P}} \Delta_{\mathcal{V}_\varepsilon}(\boldsymbol{\mu})$

3.3. Online stage

The unknown vector of coefficients $\boldsymbol{\alpha}$ is obtained by projecting the governing equations onto the reduced space $\mathcal{V}_\varepsilon$ via a Galerkin projection (Fig. 2). This leads to the following system of ordinary differential equation

$$\sum_{i=1}^{N_\varepsilon} \frac{d\alpha_j(t,\boldsymbol{\mu})}{dt} \boldsymbol{M}_{ij} = -\sum_{k=1}^{N_D} g_k(\boldsymbol{\mu}) \tilde{\boldsymbol{K}}_{ijk} + S\boldsymbol{s}_i \quad j = 1,\dots,N_\varepsilon, t \in \mathcal{I}, \boldsymbol{\mu} \in \mathcal{P} \tag{12}$$

where the matrices $\boldsymbol{M}_{ij}$, $\tilde{\boldsymbol{K}}_{ijk}$ correspond to the mass and stiffness terms described in Eqs. (8) and (10), respectively. The function $g_k(\boldsymbol{\mu})$ satisfies the linear system described in Eq. (9).

The operation count for the Online stage is given by $\mathcal{O}(N_D N_\varepsilon^2 + N_t N_\varepsilon^2 + N_\varepsilon^3)$, where $N_D N_\varepsilon^2$ accounts for assembling the $g_k(\boldsymbol{\mu})\tilde{\boldsymbol{K}}_{ijk}$ matrix, $N_t N_\varepsilon^2$ corresponds to solving the equation in time, and N_ε^3 is required for performing the LU decomposition. The key point is that the Online computational cost depends on N_D and N_ε but is independent of the full order discretization size N_h. Since $N_D, N_\varepsilon \ll N_h$, we can expect a speed up in the Online stage compared to the full order model.

The system of ODEs of Eq. (12) is implemented in the SCIANTIX code and solved over time using the Euler-Backward integration scheme to determine the time constants, which are subsequently used to reconstruct the average concentration over the volume of the columnar grain domain.

Table 1
Parameter range used to construct the training set Ξ_{train}.

Parameter	Values
Fission rate (fissions/m^3 s)	$[100;\ 5\cdot10^{19}]$
Fuel thermal conductivity (W/m K)	[0.9; 8]
Fission yield (at/fissions)	[0; 0.3]
Columnar grain length (m)	$[0.1\cdot10^{-3};\ 2\cdot10^{-3}\ ]$
Columnar grain radius (m)	$[0.75\cdot10^{-5};\ 2\cdot10^{-5}\ ]$
Temperature boundary conditions (K)	[300; 2500]

4. Results

In this section, we present the input variables chosen for the algorithms outlined in Section 3, along with the results obtained by applying the reduced order model to a reference parameter set and comparing it to the full order solution. The results are referred to the standard single-atom diffusion coefficient of [25]

$$\begin{aligned} D &= D_1 + D_2 + D_3 \\ D_1 &= 7.6\times10^{-10}\exp\left(-4.86\times10^{-19}/(k_B T)\right) \\ D_2 &= 5.64\times10^{-25}\sqrt{\dot{F}}\exp\left(-1.91\times10^{-19}/(k_B T)\right) \\ D_3 &= 8\times10^{-40}\dot{F} \end{aligned} \tag{13}$$

with k_B the Boltzmann constant (J/K).

4.1. Training set and parametric domain

The Offline phase is carried out on a training set Ξ_{train} comprising 10,000 samples, generated via random sampling with a uniform distribution across the parameter space reported in Table 1. The selected parameter ranges are based on typical operating conditions encountered in fast reactors fuelled with minor actinides bearing MOX fuels. Specifically, the irradiation experiments referenced are SUPERFACT-1 [23,24], SPHERE [40,41], and Joyo [42,43].

The lower bound of the fission rate is chosen to include low-power or near-shutdown reactor conditions, while the upper bound reflects the maximum values observed during steady-state irradiation in the fast reactors mentioned before. Fission rate zero is avoided, as it would introduce a discontinuity in the diffusion coefficient (Eq. (13)). The range of thermal conductivity accounts for variations observed in oxide fuels, including those containing minor actinides [22]. The fission gas yield spans the production of inert gases such as xenon (0.24), krypton (0.03), and helium (0.022) in UO_2 matrix, ensuring the model captures the full range of gaseous fission products.

Geometrical parameters reflect the morphology of fully developed columnar grains, with radial dimensions slightly exceeding those of as-fabricated grains (typically 10 μm), and axial lengths extending from approximately 100 μm up to several millimeters [2]. Temperature boundary conditions imposed on Γ_1, namely at the interface between the columnar grain region and the equiaxed grain region, is selected based on temperature-based criteria for restructuring zone boundaries, as provided by various institutions [2]. These criteria typically assign temperatures in the range of 2000 K to 2500 K, reflecting high-power operational conditions, with the higher values corresponding to the central region of the fuel pellet. On the other hand, lower temperatures are considered to account for low-power, when the reactor operates at significantly reduced power levels.

4.2. Full order solution

Considering an example set of parameters $\mu_{\text{reference}} = \{3\cdot10^{19}, 2.20, 0.24, 1\cdot10^{-3}, 1\cdot10^{-5}, 2000\}$, along with the time interval $\mathcal{I} = (0, 1\cdot10^7]$ and time step $\Delta t = 1\cdot10^4$, the solution of the full order problem at

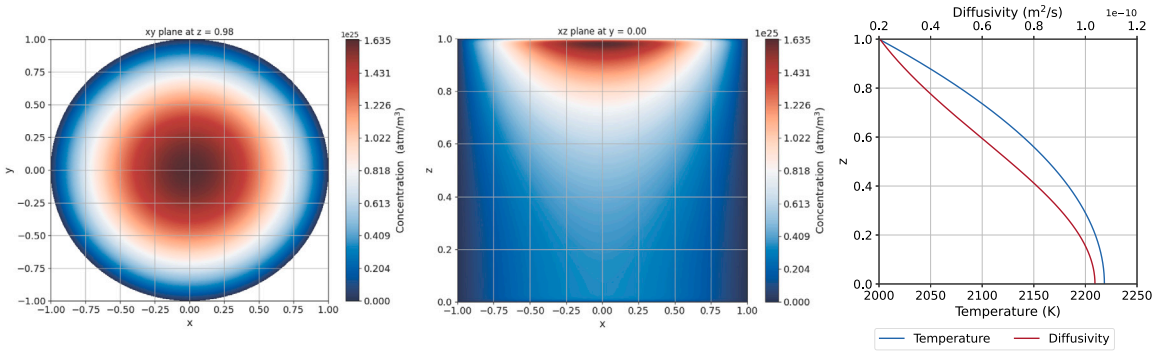

Fig. 3. On the left and center, contour plots of the concentration field evaluated with the full order model at steady state for the parameter set $\mu_{\text{reference}} = \{3 \cdot 10^{19}, 2.20, 0.24, 1 \cdot 10^{-3}, 1 \cdot 10^{-5}, 2000\}$: the left plot shows the cross-sectional view (xy-plane) at the z-coordinate corresponding to the maximum concentration value, and the center plot shows the longitudinal section (xz-plane) at $y = 0$. On the right, the temperature profile and the diffusivity profile (rescaled by the grain length) developing along the columnar grain axis.

steady-state is shown in Fig. 3, including the concentration field and the temperature and diffusivity profiles along the columnar grain axis.

The figure illustrates the diffusion process occurring within columnar grains. Along the longitudinal direction of the columnar grains, which corresponds to the radial direction along the fuel pellet, a steep temperature gradient is developed. This gradient results in higher values of the Turnbull diffusion coefficient in the inner regions of the pellet (at $z = 0$ in the plot), where the temperature is highest, gradually decreasing towards the outer regions of the pellet (at $z = 1$ in the plot). As a result, a concentration gradient forms along the grains, oriented opposite to the temperature gradient. This concentration gradient drives a flux of gas molecules towards the colder, outer regions of the grains, leading to the accumulation of gas at the grain boundaries. As shown in Fig. 3 - right, the temperature profile described by Eq. (2) results in a local gradient of approximately 220 K mm^{-1}. This value aligns with the steep thermal gradients typically encountered in MOX fuels under fast reactor conditions, as reported in [4].

4.3. Reduced basis construction

Regarding the reduced order space construction, we first pursue the DEIM procedure described in Section 3.1 to construct an affine decomposition for the Turnbull diffusion coefficient. The SVD performed on the 10,000 values of the snapshot matrix allows the construction of the function space $\mathcal{U}_D$ and the interpolation points $\boldsymbol{x}_\ell$. The number of basis functions, N_D, necessary to reconstruct the Turnbull coefficient with good accuracy, are chosen such that the mean energy of the orthogonal complement to the selected basis, normalized by the mean energy of the diffusivity fields, is lower than the specified tolerance [38], here set to $\epsilon_{\text{DEIM}} = 10^{-6}$. The averages are computed over the training set Table 1. Additionally, in this work, N_D is incremented by one to ensure robustness, even in cases where the energy condition is barely satisfied. In this specific case, the optimal number of basis functions is selected to be $N_D = 8$.

After obtaining an affine decomposition of the governing equation (Eq. (1e)), the reduced basis space $\mathcal{V}_\varepsilon$ is constructed using the POD-greedy algorithm, reported in Section 3.2, applied to the training set (Table 1). The parameter set chosen to start the first iteration of the greedy algorithm corresponds to $\mu_{\text{reference}}$. Snapshots are acquired uniformly in time during each greedy step, with a constant time step of $\Delta t = 1 \cdot 10^4$, and a total of 1000 snapshots are collected. With a tolerance set to $\epsilon_{\text{POD}} = 10^{-3}$, the resulting reduced space is spanned by 190 basis functions $\psi(\boldsymbol{x})$. The worst reconstructed parameter corresponding to this space is $\mu^\star = \{2.38 \cdot 10^{19}, 0.94, 0.29, 1.47 \cdot 10^{-3}, 1.28 \cdot 10^{-5}, 679.38\}$.

4.4. Reduced order model performance

In Fig. 4, the full order solution is compared with the reconstruction obtained using the reduced order model (Section 3.3) for the reference parameter set $\mu_{\text{reference}}$ at various time instants. The relative error remains consistently low across the domain, staying below 10^{-3}. The maximum error is observed localized in the upper and lower regions, primarily due to local effects such as the steep concentration gradient, which are more challenging for the reduced-order model to capture accurately. This error arises from the error estimator used in the POD-Greedy algorithm (Section 3.2). Specifically, the error estimator employed in this work, developed by [33], relies on a spatio-temporal energy norm expressed as a H^1 norm, which places significant weight on sharp local variations. As a result, abrupt changes in the solution contribute more heavily to the overall error, leading to reduced accuracy in these regions. Nevertheless, the error remains sufficiently small, confirming the reliability of the model in accurately reconstructing the reference solution. For this specific case, the maximum L^2 normalized error in time is attested to be around 4×10^{-4}.

In SCIANTIX, as well as in other grain-scale fission gas behaviour modules, the quantity of interest is the average fission gas concentration within a grain. In Fig. 5, we compare the time evolution of the average concentration obtained from the full order solution with the reduced order reconstructions from both the previously published model [11] and the present work. The improved ROM accurately captures the temporal evolution, maintaining excellent agreement with the FOM, with a maximum relative error on the order of 10^{-5}%. By contrast, the previously published model exhibits discrepancies up to 13%, mainly due to its simplified treatment of the nonaffine temperature dependence of the diffusion coefficient. In that work, the diffusion coefficient was approximated using a linear relation around a reference temperature, which fails to capture the nonlinear behaviour across the entire temperature range. In terms of computational performance, the present model completes 1000 time steps, achieving an online execution time of 10^{-1} s, compared to 10^{-2} s in the earlier version. This increase is a direct consequence of the larger reduced space adopted in this work — 190 POD basis functions and 8 DEIM interpolation modes, compared to only 6 modes in the earlier version — which ensures robustness and accuracy across the entire parameter domain. Nevertheless, the online cost remains negligible compared to the corresponding FEM full order simulation (tens of seconds), and, although about one order of magnitude higher than that of state-of-the-art intra-granular diffusion solvers developed for spherical geometries - such as semi-analytical algorithms (e.g., FORMAS [44]) and the spectral diffusion approach [45–47], considering 40 spatial modes - routinely used in fuel performance simulations [20,21], it still satisfies the computational-efficiency requirements for integration within such tools.

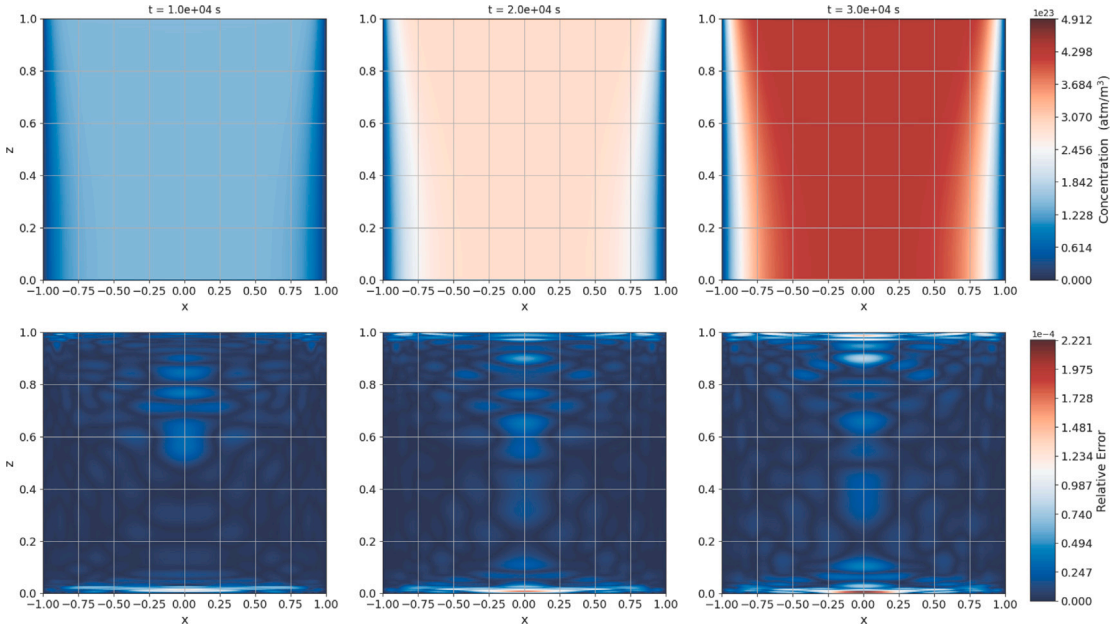

(a)

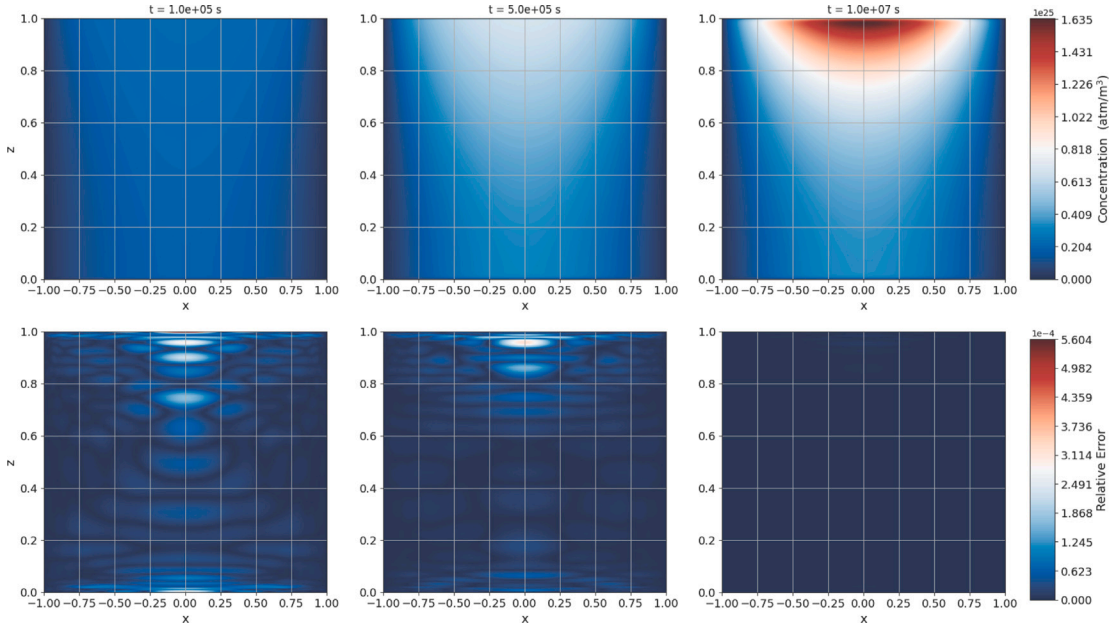

(b)

Fig. 4. Contour plots along the longitudinal section of the concentration field at different time steps, corresponding to the full order solution, along with the corresponding relative error between the concentration field obtained from the full order model and the one reconstructed using the reduced order model, for the reference parameter set $\mu_{\text{reference}}$. In (a), the plots refer to the initial time steps, while in (b), the plots refer to later time steps, up to the steady state.

5. Discussion

The SVD performed in Section 3.1 to obtain the DEIM modes provides a rank-N_D approximation hierarchy, where the leading N_D modes are retained and the remainder is neglected [38]. This behaviour is clearly visible in Fig. 6, which shows the reduction in the missing energy of the nonaffine term as the number of DEIM modes increases. For 8 basis functions the missing energy drops below the tolerance 10^{-6}, confirming that the majority of the energy has been captured and the reconstruction of the spatial diffusivity field is highly accurate for any value within the chosen training set (Table 1). To assess the accuracy of the affine approximation in reproducing the Turnbull diffusion coefficient (Eq. (13)), the maximum relative error between the exact formula and the interpolation using the 8 basis functions over the entire parameter set is $2 \cdot 10^{-3}$. This maximum error is computed on a randomly selected independent test set $\Xi_{\text{test}} \neq \Xi_{\text{training}}$, which is of the same size as the training set.

The tolerance for selecting the basis functions to affinely approximate the diffusion coefficient, $\epsilon_{\text{DEIM}} = 10^{-6}$, is set to a more stringent value compared to the tolerance chosen for selecting the POD basis functions of the reduced space $\epsilon_{\text{POD}} = 10^{-3}$. This choice aims to decouple the two sources of error as much as possible, minimizing

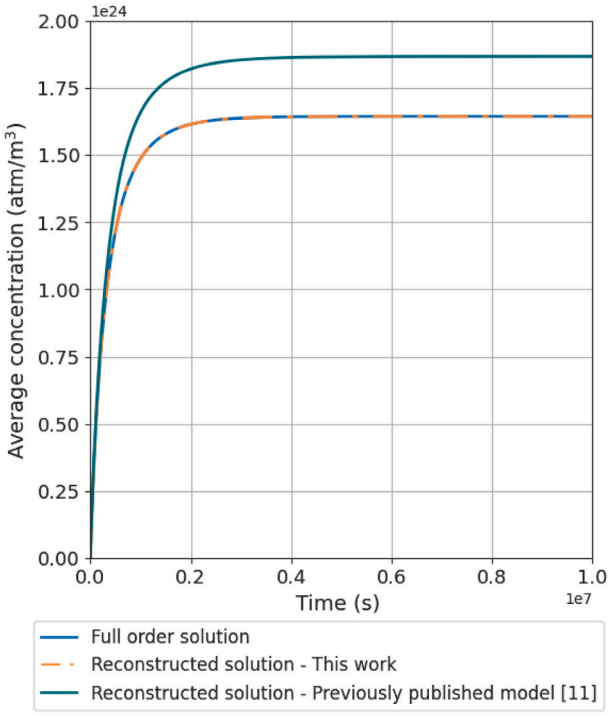

Fig. 5. Time evolution of the average fission gas concentration within the columnar grain for the reference parameter set $\mu_{\text{reference}}$. The full order model is compared with two reduced order model reconstructions: the previously published model [11] and the improved model developed in this work.

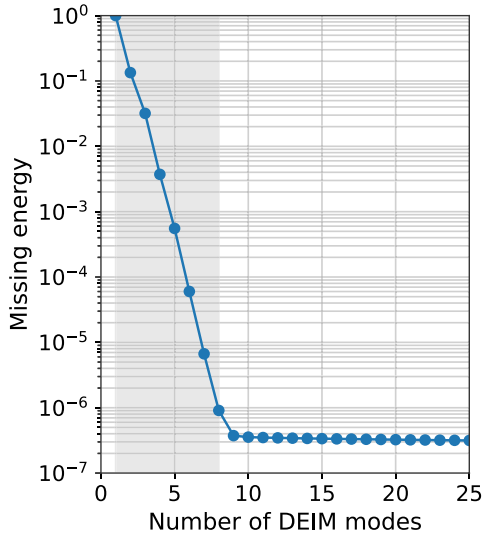

Fig. 6. Missing energy of the diffusion coefficient as a function of the number of DEIM modes. The grey-shaded region highlights the selected number of DEIM modes used in this work and the corresponding amount of retained energy.

their interaction, and also because, as shown in Fig. 6, this stringent tolerance ensures that all basis functions necessary for the affine decomposition are effectively selected.

To evaluate how well the reduced order model reproduces the full order solutions across the entire parameter set (Table 1) and to track the error associated with different choices of N_ε, in Fig. 7 presents the maximum relative error, $\eta(t, \tilde{\boldsymbol{\mu}})$, as a function of time for different

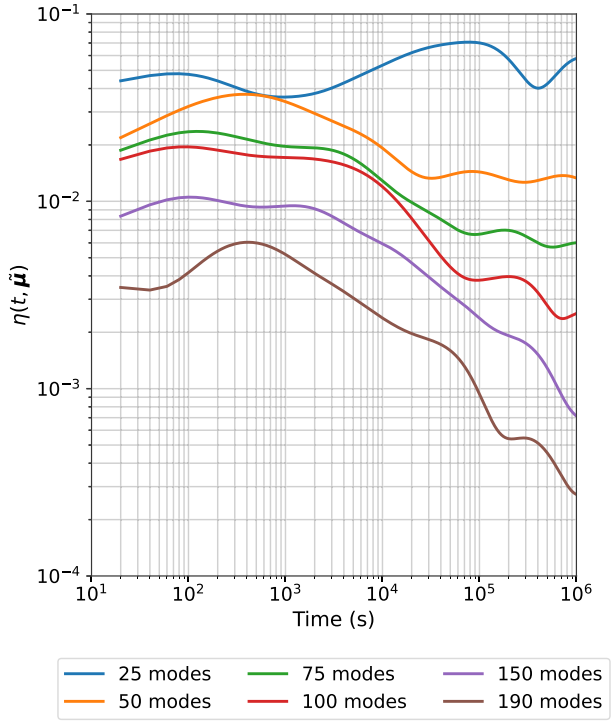

Fig. 7. Maximum L^2 relative error over time for different dimensions of the reduced space $\mathcal{V}_\varepsilon$. For each dimension, the plotted curve represents the maximum error obtained over a test set of 1000 full order solutions.

dimensions of the reduced space $\mathcal{V}_\varepsilon$. The error $\eta(t, \tilde{\boldsymbol{\mu}})$ is defined as

$$\eta(t, \boldsymbol{\mu}) = \frac{\|c^{\text{fom}}(t; \boldsymbol{\mu}) - c^{\text{rom}}(t; \boldsymbol{\mu})\|_{L^2(\tilde{\Omega})}}{\|c^{\text{fom}}(t; \boldsymbol{\mu})\|_{L^2(\tilde{\Omega})}} \tag{14}$$

where c^{rom} is computed using a varying number of POD modes and where $\tilde{\boldsymbol{\mu}}$ corresponds to the parameter associated with the maximum error in time, computed over a randomly selected independent test set of 1000 full order solutions

$$\tilde{\boldsymbol{\mu}} := \arg \max_{\boldsymbol{\mu} \in \Xi_{test}} \max_{t \in \mathcal{I}} \eta(t; \mu) \tag{15}$$

Additionally, to further assess the performance of the reduced order model, a refined time step is adopted instead of the one used for constructing the reduced space ($\Delta t = 1 \cdot 10^4$, Section 4), in order to evaluate its behaviour in scenarios characterized by faster dynamics within the training set (Table 1). Specifically, a time step of $\Delta t = 20$ is chosen, calibrated on the case with the highest diffusion coefficient.

From Fig. 7, it is clear that as the number of POD modes in the reduced order model increases, the approximation of the full order solution becomes more accurate, with the relative error decreasing significantly, thereby demonstrating the convergence of the method. However, The POD modes struggle to accurately resolve the fast dynamics and sharp changes occurring at the beginning of the simulation. This is due to the fact that these transient dynamics are underrepresented in the snapshot collection, which is evenly distributed in time. Additionally, since the error is averaged over the entire time horizon, the initial phases — which are localized in a small temporal region — are penalized, resulting in a higher relative error during these initial stages. Nevertheless, with 190 modes, the maximum error remains limited to 6×10^{-3}.

The specific problem under consideration is regular in the parameter space (Table 1), with no discontinuities —whether spatial, temporal, or parametric — and its symmetry prevents any chaotic behaviour. Moreover, being coercive and affinely decomposable within a low-dimensional linear subspace, requiring only 8 DEIM modes Fig. 6, the

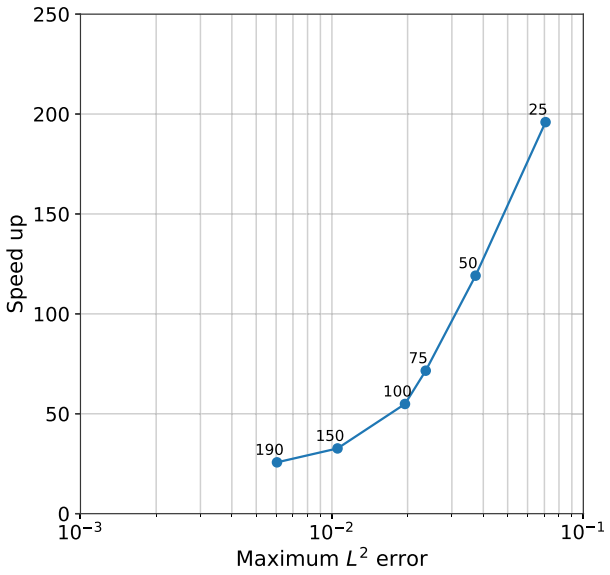

Fig. 8. Computational savings of the online stage compared to the full order simulation as a function of the maximum L^2 error associated with different modes. The numbers next to the points correspond to the number of POD modes associated with the given error and computational savings.

problem is expected to be highly reducible [48]. Consequently, a test set comprising 1000 parameter combinations is sufficient to provide a well-generalized assessment of the model, effectively covering the variability within the parameter space.

The full order simulation and the reduced order modelling computations are performed using Python on a MacBook Pro with an M2 chip and 16 GB of RAM. The construction of the reduced model incurs an offline cost of approximately 19 h. This includes the time for computing the full order solutions (2 min), the time for calculating the POD basis functions and assembling the reduced basis model tensors (2 min), and the time for calculating the worst-reconstructed parameter, $\boldsymbol{\mu}^{\star}$, at each greedy step for the error estimator (18 h 56′). The computational cost of a finite element solution with 50 000 iterations is approximately 50 s. In contrast, the surrogate model obtained using $N_D = 8$ and $N_\epsilon = 190$ basis functions produces a solution in only 2 s (online cost), which is about 1/25th of the time required for the full order solution. Fig. 8 illustrates the speed up achieved during the online phase compared to solving the full order simulation as a function of the maximum relative error in the L^2 norm, namely the maximum $\eta(t, \tilde{\boldsymbol{\mu}})$ shown in Fig. 7, associated with different dimensions of the reduced space. As the number of modes increases, the error decreases, and the computational savings gradually decrease as well, reflecting the trade-off between accuracy and computational efficiency.

6. Conclusions and perspectives

This work addresses the problem of modelling intra-granular fission gas diffusion in columnar grains, overcoming the limitations of traditional models that assume spherical grain geometry and neglect temperature gradients. By employing reduced order techniques, the model accounts for the non-spheroidal shape of the grains and the non-uniform temperature distribution, while maintaining a computational cost in line with its application in fuel performance codes.

We present a time-dependent reduced order model developed for parabolic partial differential equations governing the concentration and temperature fields, with a nonaffine parametric dependence embedded in the diffusion coefficient. The present formulation builds upon our previously published reduced order framework by introducing a discrete empirical interpolation method (DEIM) to efficiently handle the nonlinearity in the diffusion coefficient and a proper orthogonal decomposition (POD)-greedy algorithm for optimal mode selection over a broader parameter space.

The accuracy of the reduced order model with 190 modes is assessed through detailed error analysis attesting a maximum L^2 error over time of $6 \cdot 10^{-3}$ when tested on an independent parameter set. The computational savings in the online phase are substantial, achieving up to a $\mathcal{O}(25)$ reduction in time compared to the full order solution. Compared to the previously published version, the present formulation achieves higher accuracy and robustness while preserving computational efficiency, thereby demonstrating the viability of the proposed approach for large-scale fuel performance simulations and making it a powerful tool for integral-scale evaluation.

The model is implemented in the 0D grain-scale fission gas behaviour module SCIANTIX, where the average concentration within the columnar grain domain is reconstructed as the key figure of merit. The final aim is to incorporate and assess this model within a fuel performance code for comprehensive fuel pin analysis. Notably, integrating this reduced order model into the fuel performance framework requires a dedicated interface. This is because the size of columnar grains, ranging from hundreds of microns to nearly a millimeter, exceeds the typical mesh cell size used in fuel performance simulations — unlike unrestructured spherical grains, which are only a few microns in size. As a result, the model cannot be invoked at each mesh element or quadrature point. Moreover, while 190 modes may appear excessively high — potentially suggesting a nearly full order model with a significant computational cost - the impact on fuel performance simulations remains limited. The columnar grain structure occupies only a specific portion of the fuel pellet, meaning that in pin-scale simulations, this model is invoked far less frequently than others. This reduced number of calls allows for a higher number of modes to be employed, ensuring an accurate representation of the phenomenon without excessively increasing the computational burden.

In this study, the assumption of a uniform thermal conductivity and uniform fission rate within the columnar grain region are recognized as a model limitation. Future developments could consider the radial variation of both of them to improve the physical accuracy. An additional refinement could involve using temperature profiles directly computed by fuel performance codes, rather than calculating them within the model itself. In such a case, the affine decomposition training would need to be re-performed using a training set of temperature profiles generated by the performance code. However, this modification would not alter the structure of the reduced order model: the method itself remains valid and applicable regardless of the temperature profile used. This highlights the flexibility of the proposed approach, which can accommodate different physical assumptions without changing its underlying framework.

Reduced order modelling techniques represent a cutting-edge topic in applied mathematics, yet their potential remains largely unexplored in the field of fuel performance. This application of reduced order models as grain-scale tools represents one of the first achievements in this direction and can be extended beyond fission gas behaviour. In the future, the modelling procedure proves to be well-suited for extension to other grain morphologies. While grain-scale models typically assume single grains to have a spherical shape, a more realistic approach would consider their actual polyhedral structure [49]. Unlike spheres, polyhedral grains have distinct edge and corner regions that alter diffusion pathways and gas concentration gradients, making the spherical assumption insufficient to capture variations in gas diffusion [50]. Developing a specific diffusion model for grains with a non-spherical shape would allow for a more accurate interpretation of irradiation experiments conducted on single grains.

CRediT authorship contribution statement

M. Di Gennaro: Writing – original draft, Visualization, Software, Methodology, Formal analysis, Data curation, Conceptualization. **D. Pizzocri:** Writing – review & editing, Supervision, Methodology, Conceptualization. **F.A.B. Silva:** Writing – original draft, Visualization, Supervision, Software, Investigation, Formal analysis, Conceptualization. **G. Zullo:** Writing – review & editing, Supervision, Software, Data curation. **S. Lorenzi:** Writing – review & editing, Supervision, Methodology, Conceptualization. **A. Cammi:** Writing – review & editing, Supervision, Conceptualization. **L. Luzzi:** Writing – review & editing, Writing – original draft, Supervision, Funding acquisition, Conceptualization.

Declaration of competing interest

The authors declare that they have no known competing financial interests or personal relationships that could have appeared to influence the work reported in this paper.

Acknowledgements

This work has received funding from the Euratom research and training programme 2021–2027 through the OperaHPC project under grant agreement n° 101061453.

Data availability

Data will be made available on request.

References

[1] J.R. MacEwan, V.B. Lawson, Grain growth in sintered uranium dioxide: II, columnar grain growth, J. Am. Ceram. Soc. 45 (1962) http://dx.doi.org/10.1111/j.1151-2916.1962.tb11027.x.
[2] D.R. Olander, Fundamental Aspects of Nuclear Reactor Fuel Elements, Technical lnformation Center Energy Research and Development Administration, 1976.
[3] S. Novascone, P. Medvedev, J.W. Peterson, Y. Zhang, J. Hales, Modeling porosity migration in LWR and fast reactor MOX fuel using the finite element method, J. Nucl. Mater. 508 (2018) http://dx.doi.org/10.1016/j.jnucmat.2018.05.041.
[4] Y. Guerin, Fuel performance of fast spectrum oxide fuel, in: Comprehensive Nuclear Materials, Vol. 1–5, 2012, http://dx.doi.org/10.1016/B978-0-08-056033-5.00043-4, Chapter 2.21.
[5] I.W. Vance, P.C. Millett, Phase-field simulations of pore migration and morphology change in thermal gradients, J. Nucl. Mater. 490 (2017) http://dx.doi.org/10.1016/j.jnucmat.2017.04.027.
[6] D.R. Olander, The materials of fast breeder reactors, Naturwissenschaften 67 (1980) http://dx.doi.org/10.1007/BF01054687.
[7] R. Parrish, A. Aitkaliyeva, A review of microstructural features in fast reactor mixed oxide fuels, 2018, http://dx.doi.org/10.1016/j.jnucmat.2018.05.076.
[8] D. Pizzocri, A. Cechet, L. Cognini, A. Magni, A. Schubert, P.V. Uffelen, T. Wiss, L. Luzzi, A modelling methodology for the description of helium behaviour accounting for the grain-size distribution, Nucl. Eng. Des. 411 (2023) http://dx.doi.org/10.1016/j.nucengdes.2023.112426.
[9] U.M. El-Saied, D.R. Olander, Fission gas release during grain growth in a microstructure with a distribution of grain sizes, J. Nucl. Mater. 207 (1993) http://dx.doi.org/10.1016/0022-3115(93)90274-3.
[10] A.H. Booth, A method of calculating fission gas diffusion from UO_2 fuel and its application to the X-2-f loop test, 1957, URL https://www.osti.gov/biblio/4331839.
[11] D. Pizzocri, M. Di Gennaro, T. Barani, F.A. Silva, G. Zullo, S. Lorenzi, A. Cammi, A reduced order model for fission gas diffusion in columnar grains, Nucl. Eng. Technol. 55 (2023) http://dx.doi.org/10.1016/j.net.2023.07.013.
[12] S. Chaturantabut, D.C. Sorensen, Nonlinear model reduction via discrete empirical interpolation, SIAM J. Sci. Comput. 32 (2010) http://dx.doi.org/10.1137/090766498.
[13] G. Berkooz, P. Holmes, J.L. Lumley, The proper orthogonal decomposition in the analysis of turbulent flows, Annu. Rev. Fluid Mech. 25 (1993) 539–575, URL https://api.semanticscholar.org/CorpusID:16960127.
[14] S. Lorenzi, A. Cammi, L. Luzzi, G. Rozza, POD-Galerkin method for finite volume approximation of Navier–Stokes and RANS equations, Comput. Methods Appl. Mech. Engrg. 311 (2016) 151–179, http://dx.doi.org/10.1016/j.cma.2016.08.006.
[15] G. Stabile, S. Hijazi, A. Mola, S. Lorenzi, G. Rozza, POD-Galerkin reduced order methods for CFD using finite volume discretisation: vortex shedding around a circular cylinder, Commun. Appl. Ind. Math. 8 (2017) 210–236, http://dx.doi.org/10.1515/caim-2017-0011.
[16] G. Pastore, L.P. Swiler, J.D. Hales, S.R. Novascone, D.M. Perez, B.W. Spencer, L. Luzzi, P.V. Uffelen, R.L. Williamson, Uncertainty and sensitivity analysis of fission gas behavior in engineering-scale fuel modeling, J. Nucl. Mater. 456 (2015) 398–408, http://dx.doi.org/10.1016/j.jnucmat.2014.09.077.
[17] F. Hecht, New development in freefem+, J. Numer. Math. 20 (2012) http://dx.doi.org/10.1515/jnum-2012-0013.
[18] D. Pizzocri, T. Barani, L. Luzzi, SCIANTIX: A new open source multi-scale code for fission gas behaviour modelling designed for nuclear fuel performance codes, J. Nucl. Mater. 532 (2020) 152042, http://dx.doi.org/10.1016/j.jnucmat.2020.152042.
[19] G. Zullo, D. Pizzocri, L. Luzzi, The SCIANTIX code for fission gas behaviour: Status, upgrades, separate-effect validation, and future developments, J. Nucl. Mater. 587 (2023) 154744, http://dx.doi.org/10.1016/J.JNUCMAT.2023.154744.
[20] G. Zullo, D. Pizzocri, A. Magni, P. Van Uffelen, A. Schubert, L. Luzzi, Towards grain-scale modelling of the release of radioactive fission gas from oxide fuel. Part II: Coupling SCIANTIX with TRANSURANUS, Nucl. Eng. Technol. 54 (2022) 4460–4473, http://dx.doi.org/10.1016/J.NET.2022.07.018.
[21] G. Zullo, D. Pizzocri, A. Scolaro, P. Van Uffelen, F. Feria, L. Herranz, L. Luzzi, Integral-scale validation of the SCIANTIX code for light water reactor fuel rods, J. Nucl. Mater. 601 (2024) 155305, http://dx.doi.org/10.1016/j.jnucmat.2024.155305, URL https://www.sciencedirect.com/science/article/pii/S0022311524004070.
[22] M. Di Gennaro, A. Magni, M. Guarnieri, D. Pizzocri, L. Luzzi, C. Guéneau, P. Van Uffelen, Modelling and assessment of thermophysical properties of Am-bearing fuels for transmutation purposes in fast reactors, Prog. Nucl. Energy 185 (2025) 105698, http://dx.doi.org/10.1016/j.pnucene.2025.105698, URL https://www.sciencedirect.com/science/article/pii/S0149197025000964.
[23] L. Luzzi, T. Barani, B. Boer, L. Cognini, A.D. Nevo, M. Lainet, S. Lemehov, A. Magni, V. Marelle, B. Michel, D. Pizzocri, A. Schubert, P.V. Uffelen, M. Bertolus, Assessment of three European fuel performance codes against the SUPERFACT-1 fast reactor irradiation experiment, Nucl. Eng. Technol. 53 (2021) 3367–3378, http://dx.doi.org/10.1016/j.net.2021.04.010.
[24] L. Luzzi, T. Barani, B. Boer, A.D. Nevo, M. Lainet, S. Lemehov, A. Magni, V. Marelle, B. Michel, D. Pizzocri, A. Schubert, P.V. Uffelen, M. Bertolus, Assessment of INSPYRE-extended fuel performance codes against the SUPERFACT-1 fast reactor irradiation experiment, Nucl. Eng. Technol. 55 (2023) 884–894, http://dx.doi.org/10.1016/j.net.2022.10.038.
[25] J.A. Turnbull, R.J. White, C. Wise, The diffusion coefficient for fission gas atoms in uranium dioxide, 1989, URL https://inis.iaea.org/search/search.aspx?orig_q=RN:21003206.
[26] K. Lassmann, TRANSURANUS: a fuel rod analysis code ready for use, Nucl. Mater. Fission React. (1992) 295–302, http://dx.doi.org/10.1016/b978-0-444-89571-4.50046-3.
[27] A. Magni, A.D. Nevo, L. Luzzi, D. Rozzia, M. Adorni, A. Schubert, P.V. Uffelen, The TRANSURANUS fuel performance code, in: J. Wang, X. Li, C. Allison, J. Hohorst (Eds.), Nuclear Power Plant Design and Analysis Codes, Woodhead Publishing, 2021, pp. 161–205, http://dx.doi.org/10.1016/B978-0-12-818190-4.00008-5.
[28] K.J. Geelhood, W.G. Luscher, P. Raynaud, I.E. Porter, FRAPCON-4.0: A Computer Code for the Calculation of Steady-State, Thermal-Mechanical Behavior of Oxide Fuel Rods for High Burnup, 2015.
[29] H.J. Matzke, Gas release mechanisms in UO 2 —a critical review, Radiat. Eff. 53 (1980) 219–242, http://dx.doi.org/10.1080/00337578008207118.
[30] M.V. Speight, A calculation on the migration of fission gas in material exhibiting precipitation and re-solution of gas atoms under irradiation, Nucl. Sci. Eng. 37 (1969) 180–185, http://dx.doi.org/10.13182/nse69-a20676.
[31] GitHub repository, SCIANTIX official GitHub repository, 2023, https://github.com/sciantix/sciantix-official.
[32] A. Quarteroni, A. Manzoni, F. Negri, Reduced basis methods for partial differential equations: An introduction, 2015, http://dx.doi.org/10.1007/978-3-319-15431-2.
[33] M.A. Grepl, A.T. Patera, A posteriori error bounds for reduced-basis approximations of parametrized parabolic partial differential equations, Math. Model. Numer. Anal. 39 (2005) http://dx.doi.org/10.1051/m2an:2005006.
[34] B. Haasdonk, Convergence rates of the pod—greedy method, Math. Model. Numer. Anal. 47 (2013) http://dx.doi.org/10.1051/m2an/2012045.
[35] B. Haasdonk, M. Ohlberger, Reduced basis method for finite volume approximations of parametrized linear evolution equations, Math. Model. Numer. Anal. 42 (2008) http://dx.doi.org/10.1051/m2an:2008001.
[36] J.A. Turnbull, C.A. Friskney, J.R. Findlay, F.A. Johnson, A.J. Walter, The diffusion coefficients of gaseous and volatile species during the irradiation of uranium dioxide, J. Nucl. Mater. 107 (1982) 168–184, http://dx.doi.org/10.1016/0022-3115(82)90419-6.

[37] Y. Maday, N.C. Nguyen, A.T. Patera, G.S. Pau, A general multipurpose interpolation procedure: The magic points, Commun. Pure Appl. Anal. 8 (2009) http://dx.doi.org/10.3934/cpaa.2009.8.383.

[38] S.L. Brunton, J.N. Kutz, Data-driven science and engineering, 2019, http://dx.doi.org/10.1017/9781108380690.

[39] G. Rozza, M. Hess, G. Stabile, M. Tezzele, F. Ballarin, Basic ideas and tools for projection-based model reduction of parametric partial differential equations, 2020, http://dx.doi.org/10.1515/9783110671490-001.

[40] M. Lainet, L. Luzzi, A. Magni, D. Pizzocri, M. Di Gennaro, P. Van Uffelen, A. Schubert, E. D'Agata, V. Romanello, A. Rineiski, K. Sturm, S. Van Til, F. Charpin, A. Fedorov, Advanced interpretation of the SPHERE irradiation experiment with neutronics and fuel performance codes, Nucl. Eng. Technol. 56 (11) (2024) 4734–4747, http://dx.doi.org/10.1016/j.net.2024.06.037, URL https://www.sciencedirect.com/science/article/pii/S1738573324002973.

[41] M. Lainet, M. Di Gennaro, A. Magni, D. Pizzocri, L. Luzzi, A. Schubert, P. Van Uffelen, E. D'Agata, V. Romanello, A. Rineiski, K. Sturm, Results of the Fuel Performance Code Benchmark Assessment, Patricia Deliverable d5.3, PATRICIA Consortium, 2024.

[42] K. Maeda, S. Sasaki, M. Kato, Y. Kihara, Short-term irradiation behavior of minor actinide doped uranium plutonium mixed oxide fuels irradiated in an experimental fast reactor, J. Nucl. Mater. 385 (2009) http://dx.doi.org/10.1016/j.jnucmat.2008.12.041.

[43] M.S. Veshchunov, New models for UO2 fuel structure evolution under irradiation in fast reactors, J. Nucl. Mater. 415 (2011) http://dx.doi.org/10.1016/j.jnucmat.2011.05.046.

[44] K. Lassmann, H. Benk, Numerical algorithms for intragranular fission gas release, J. Nucl. Mater. 280 (2000) http://dx.doi.org/10.1016/S0022-3115(00)00044-1.

[45] D. Pizzocri, C. Rabiti, L. Luzzi, T. Barani, P.V. Uffelen, G. Pastore, PolyPole-1: An accurate numerical algorithm for intra-granular fission gas release, J. Nucl. Mater. 478 (2016) 333–342, http://dx.doi.org/10.1016/j.jnucmat.2016.06.028.

[46] G. Pastore, D. Pizzocri, C. Rabiti, T. Barani, P.V. Uffelen, L. Luzzi, An effective numerical algorithm for intra-granular fission gas release during non-equilibrium trapping and resolution, J. Nucl. Mater. 509 (2018) http://dx.doi.org/10.1016/j.jnucmat.2018.07.030.

[47] G. Zullo, D. Pizzocri, L. Luzzi, On the use of spectral algorithms for the prediction of short-lived volatile fission product release: Methodology for bounding numerical error, Nucl. Eng. Technol. 54 (4) (2022) 1195–1205, http://dx.doi.org/10.1016/j.net.2021.10.028, URL https://www.sciencedirect.com/science/article/pii/S1738573321006148.

[48] M. Ohlberger, S. Rave, Reduced basis methods: Success, limitations and future challenges, 2015, ArXiv: Numerical Analysis.

[49] A. Claisse, P. Van Uffelen, Towards the inclusion of open fabrication porosity in a fission gas release model, J. Nucl. Mater. 466 (2015) http://dx.doi.org/10.1016/j.jnucmat.2015.08.022.

[50] A. Pagani, D. Pizzocri, G. Zullo, P. Van Uffelen, L. Luzzi, An AI-enhanced model of athermal fission gas release in Sciantix, SSRN Electron. J. (2025) http://dx.doi.org/10.2139/ssrn.5170480.